Electronic evidence of an insulator–superconductor crossover in single-layer FeSe/$SrTiO_3$ films

Junfeng He[a,1], Xu Liu[a,1], Wenhao Zhang[b,c,1], Lin Zhao[a,1], Defa Liu[a], Shaolong He[a], Daixiang Mou[a], Fangsen Li[c], Chenjia Tang[b,c], Zhi Li[c], Lili Wang[c], Yingying Peng[a], Yan Liu[a], Chaoyu Chen[a], Li Yu[a], Guodong Liu[a], Xiaoli Dong[a], Jun Zhang[a], Chuangtian Chen[d], Zuyan Xu[d], Xi Chen[b], Xucun Ma[c,2], Qikun Xue[b,2], and X. J. Zhou[a,e,2]

[a]National Lab for Superconductivity, Beijing National Laboratory for Condensed Matter Physics, Institute of Physics, Chinese Academy of Sciences, Beijing 100190, China; [b]State Key Lab of Low-Dimensional Quantum Physics, Department of Physics, Tsinghua University, Beijing 100084, China; [c]Beijing National Laboratory for Condensed Matter Physics, Institute of Physics, Chinese Academy of Sciences, Beijing 100190, China; [d]Technical Institute of Physics and Chemistry, Chinese Academy of Sciences, Beijing 100190, China; and [e]Collaborative Innovation Center of Quantum Matter, Beijing 100871, China

Edited* by E. W. Plummer, Louisiana State University, Baton Rouge, LA, and approved November 13, 2014 (received for review August 17, 2014)

In high-temperature cuprate superconductors, it is now generally agreed that superconductivity is realized by doping an antiferromagnetic Mott (charge transfer) insulator. The doping-induced insulator-to-superconductor transition has been widely observed in cuprates, which provides important information for understanding the superconductivity mechanism. In the iron-based superconductors, however, the parent compound is mostly antiferromagnetic bad metal, raising a debate on whether an appropriate starting point should go with an itinerant picture or a localized picture. No evidence of doping-induced insulator–superconductor transition (or crossover) has been reported in the iron-based compounds so far. Here, we report an electronic evidence of an insulator–superconductor crossover observed in the single-layer FeSe film grown on a $SrTiO_3$ substrate. By taking angle-resolved photoemission measurements on the electronic structure and energy gap, we have identified a clear evolution of an insulator to a superconductor with increasing carrier concentration. In particular, the insulator–superconductor crossover in FeSe/$SrTiO_3$ film exhibits similar behaviors to that observed in the cuprate superconductors. Our results suggest that the observed insulator–superconductor crossover may be associated with the two-dimensionality that enhances electron localization or correlation. The reduced dimensionality and the interfacial effect provide a new pathway in searching for new phenomena and novel superconductors with a high transition temperature.

single-layer FeSe/$SrTiO_3$ films | insulator-to-superconductor crossover | ARPES

The iron-based superconductors (1–4) represent the second class of high-temperature superconductors after the discovery of the first class of high-temperature cuprate superconductors. It is now generally agreed that the superconductivity in cuprates is realized by doping a Mott (charge transfer) insulator (5). In the iron-based superconductors, however, the parent compounds mostly exhibit a poor metallic behavior with an antiferromagnetic order, thus raising a debate on whether an appropriate starting point should go with an itinerant picture or a localized picture (6–18), particularly whether the picture of doping a Mott insulator is relevant to the iron-based superconductors (1, 3, 11, 16, 17). Some theoretical calculations indicate that the iron-based superconductors may be in proximity to a Mott insulator (11, 16, 17), and attempts have also been made to unify cuprates and iron-based superconductors in theory (18). However, so far no clear experimental evidence of doping (or carrier concentration)-induced insulator–superconductor transition (or crossover) has been reported in the iron-based superconductors.

The latest discovery of possible high-temperature superconductivity in the single-layer FeSe films grown on a $SrTiO_3$ substrate has attracted much attention both experimentally (19–27) and theoretically (28–32). The reduced dimensionality with enhanced interfacial effect makes this system distinct from its bulk counterpart. First, it has a simple crystal structure that consists of a single-layer Se-Fe-Se unit, which is an essential building block of the iron-based superconductors (19). Second, the superconducting single-layer FeSe/$SrTiO_3$ film possesses a distinct electronic structure that exhibits only electron pockets near the Brillouin zone corner without any Fermi crossing near the zone center (20–22). In particular, it was found that annealing in vacuum can tune the carrier concentration of the FeSe/$SrTiO_3$ films (21, 33), thus providing a good opportunity to investigate its carrier-dependent behaviors.

In this paper, to our knowledge, we report the first observation of an insulator–superconductor crossover in the iron-based superconductors by performing systematic angle-resolved photoemission (ARPES) measurements on the single-layer FeSe/$SrTiO_3$ films at various carrier concentrations. At a very low carrier concentration, the spectral weight near the Fermi level is suppressed, accompanied with the opening of an insulating energy gap. When the carrier concentration increases, the spectral weight begins to fill in the insulating gap, resulting in a decrease in gap size with the formation and sharpening of the peak at the

Significance

The doping-induced insulator-to-superconductor transition has been widely observed in cuprates, which provides important information for understanding the superconductivity mechanism. However, in the iron-based superconductors, no evidence of doping-induced insulator–superconductor transition (or crossover) has been reported so far. In this paper, to our knowledge, we report the first electronic evidence of an insulator–superconductor crossover observed in the single-layer FeSe film grown on a $SrTiO_3$ substrate, which exhibits similar behaviors to that observed in the cuprate superconductors. The observed insulator–superconductor crossover may be associated with the two-dimensionality that enhances electron localization or correlation. The reduced dimensionality and the interfacial effect provide a new pathway in searching for new phenomena and novel superconductors with a high transition temperature.

Author contributions: X.J.Z., Q.K.X., X.C.M., and J.F.H. proposed and designed the research; W.H.Z., F.S.L., C.J.T., Z.L., L.L.W., X.C., X.C.M., and Q.K.X. contributed to molecular beam epitaxy thin film preparation; J.F.H., X.L., L.Z., D.F.L., S.L.H., D.X.M., Y.Y.P., Y.L., C.Y.C., L.Y., G.D.L., X.L.D., J.Z., C.T.C., Z.Y.X., and X.J.Z. contributed to the development and maintenance of laser-based angle-resolved photoemission spectroscopy (ARPES) system; J.F.H., X.L., L.Z., D.F.L., S.L.H. carried out the ARPES experiment; J.F.H., X.L., L.Z., D.F.L., S.L.H., and X.J.Z. analyzed the data; J.F.H. and X.J.Z. wrote the paper with X.L., L.Z., D.F.L., S.L.H., X.C.M., and Q.K.X.

The authors declare no conflict of interest.

*This Direct Submission article had a prearranged editor.

[1]J.F.H., X.L., W.H.Z., and L.Z. contributed equally to this work.

[2]To whom correspondence may be addressed. Email: XJZhou@aphy.iphy.ac.cn, qkxue@mail.tsinghua.edu.cn, or xcma@aphy.iphy.ac.cn.

This article contains supporting information online at www.pnas.org/lookup/suppl/doi:10.1073/pnas.1414094112/-/DCSupplemental.

PHYSICS

Fermi level. Eventually, when the carrier concentration increases to a critical value, the insulating gap closes and superconductivity starts to emerge. The overall evolution in the single-layer FeSe/$SrTiO_3$ film is quite similar to the insulator–superconductor transition observed in the cuprate superconductors (34–38). Our observations have established a clear case that an insulator–superconductor crossover takes place with increasing carrier concentration in a 2D iron-based superconductor. The similarities between the current observations and those in cuprates provide new insights in understanding the superconductivity mechanism in these systems. The observed insulator–superconductor crossover in the single-layer FeSe/$SrTiO_3$ film points to the significant role of the reduced dimensionality in dictating the physical properties and superconductivity.

Results

The as-grown FeSe/$SrTiO_3$ films were consecutively annealed in vacuum. During the annealing process, it was found that two different phases can be identified in the single-layer FeSe/$SrTiO_3$ films by their distinct electronic structures: The initial N phase in the as-grown sample possesses an electronic structure that bears resemblance to that observed in the parent compound of $BaFe_2As_2$ in its magnetic state (21, 39), and the final S phase in the sufficiently annealed sample shows only electron pockets near the (π,π) zone corners (21). The N phase decreases with the vacuum annealing accompanied by an increase in the S phase; they coexist in the intermediate annealing process (21). In this work, we will concentrate on the S phase and report our observation of an insulator–superconductor crossover with increasing carrier concentration in this S phase. Because the S phase shows only electron pockets near the M(π,π) points, the carrier concentration of the S phase can be determined by the measured area of the electron Fermi pockets (*SI Appendix*, Fig. S1). Different annealing sequences lead to different carrier concentrations of the S phase. For convenience, we will label the samples annealed at different sequences with the carrier concentration x hereafter.

The primary question we will address in this work is, as soon as the S phase emerges with vacuum annealing, whether it is insulating, metallic, or superconducting. For this purpose, we take advantage of the photoemission matrix element effect to selectively probe the electronic structure of the S phase even when it coexists with the N phase in the intermediate annealing process. We find that, using a proper measurement geometry, the electronic structure along a momentum cut near M2(−π,π) is dominated by the signal of the S phase, whereas the signal along a momentum cut near M3(−π,−π) is dominated by the N phase (*SI Appendix*, Fig. S2). This makes it possible for us to focus on the signal of the S phase, as presented below.

Fig. 1 shows the band structure evolution with the carrier concentration for the S phase in the single-layer FeSe/$SrTiO_3$ films (Fig. 1 *A*–*G*). The measurement was performed along the momentum cut shown in Fig. 1*O* near the M2 point at a temperature of ∼20 K. For comparison, the band structure of the La-doped $Bi_2Sr_2CuO_{6+\delta}$ (La-Bi2201) at various doping levels measured along the (0,0)-(π,π) nodal cut (Fig. 1*P*) is also presented in Fig. 1 *H*–*N*. For the La-Bi2201 system, it has been shown that in the heavily underdoped region, there is an insulator–superconductor transition that occurs near the doping level of ∼0.10: below this doping level, there is a gap near the nodal region and the entire Fermi surface is gapped (35). As seen from Fig. 1, at a very low carrier concentration, the spectral weight of the electron-like bands in the S phase of the single-layer FeSe/$SrTiO_3$ film is rather weak (Fig. 1*A*). It gets stronger with the increasing carrier concentration. The band structure evolution with carrier concentration in the S phase is quite similar to that observed in La-Bi2201 (35).

Photoemission spectra [energy distribution curves (EDCs)] of the S phase in the single-layer FeSe/$SrTiO_3$ film measured at the Fermi momentum of the electron-like band (k_{FR} in Fig. 2*A*) at ∼20 K are shown in Fig. 2*B* (for original EDCs, see *SI Appendix*, Fig. S3). At a carrier concentration lower than 0.073, the corresponding EDC shows little spectral weight at the Fermi level. When the carrier concentration increases, a peak first emerges near the Fermi level, and then gets stronger and becomes a well-defined

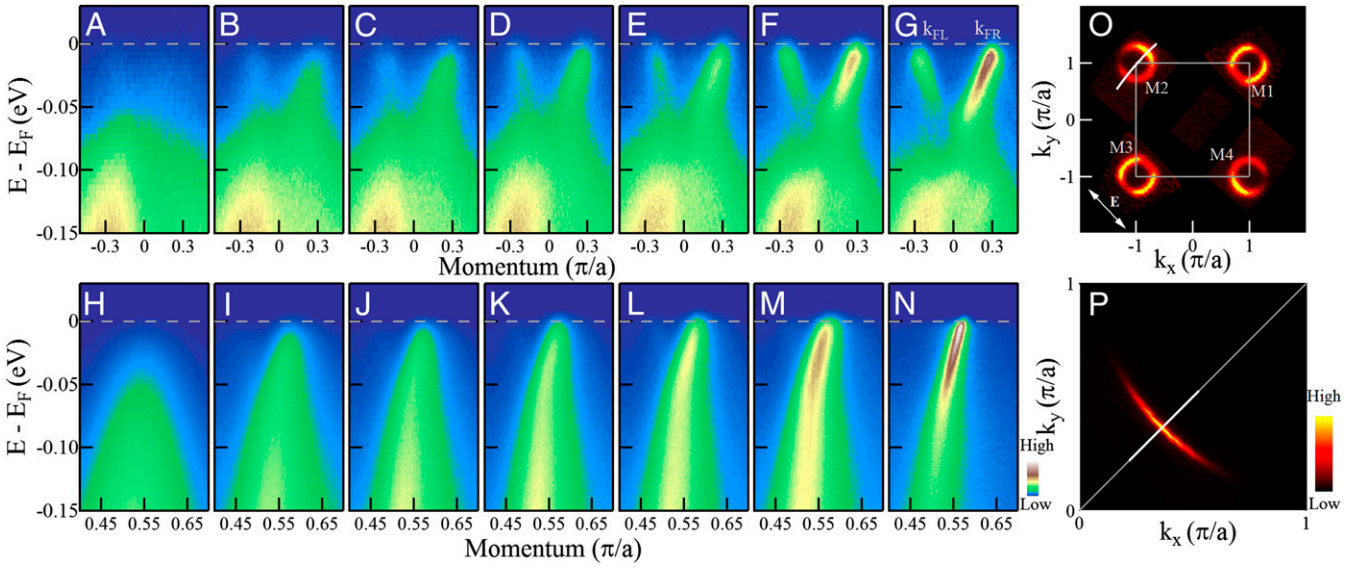

Fig. 1. Doping evolution of band structure of the S phase in the single-layer FeSe/$SrTiO_3$ film and the comparison with that in La-Bi2201. (*A*–*G*) Band structures of the S phase corresponding to carrier concentrations of <0.073, 0.073, 0.076, 0.087, 0.089, 0.098, and 0.114, respectively. The measurements were performed at a temperature of ∼20 K along a momentum cut near M2, as shown in *O* on a typical Fermi surface mapping of the 0.114 sample (21). For comparison, the band structure evolution of La-Bi2201 is shown in *H*–*N*, which correspond to doping levels of P = 0.03, 0.04, 0.055, 0.07, 0.08, 0.10, and 0.16, respectively. The measurements were performed at a temperature of ∼15 K along a nodal momentum cut as shown in *P* on a Fermi surface mapping of La-Bi2201 with P = 0.16 (35).

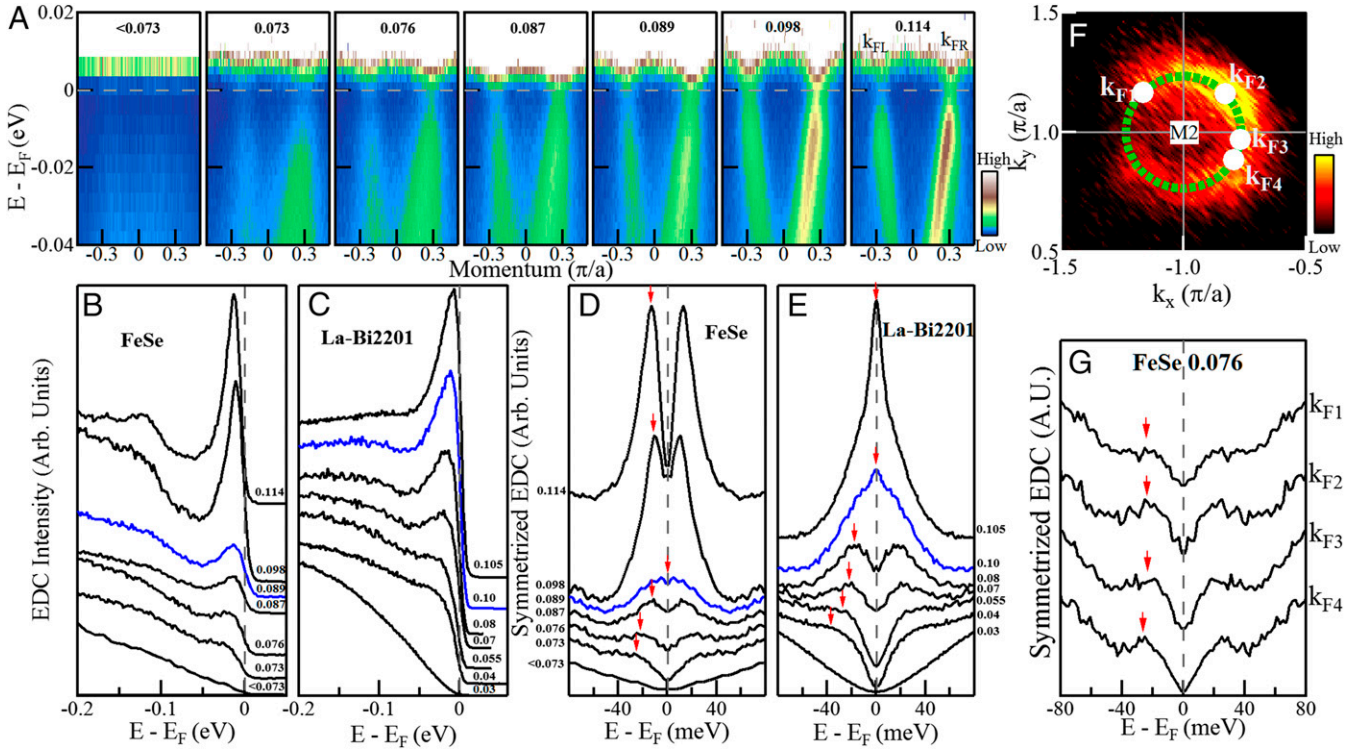

Fig. 2. Doping evolution of the photoemission spectra and the energy gap of the S phase in the single-layer FeSe/$SrTiO_3$ film and its comparison with that in La-Bi2201 system. (*A*) Photoemission intensity plots of the S phase corresponding to carrier concentrations of <0.073, 0.073, 0.076, 0.087, 0.089, 0.098, and 0.114, respectively, along the momentum cut shown in Fig. 1*O*. The Fermi distribution function is divided out to observe the opening of the energy gap. (*B*) Original EDCs at the Fermi momentum (k_{FR}) marked in *A* (on 0.114 sample). The corresponding symmetrized EDCs are shown in *D*. The EDCs are labeled by the corresponding carrier concentrations. (*C*) Original EDCs at k_F for La-Bi2201 along the momentum cut of the nodal direction (Fig. 1*P*). The corresponding symmetrized EDCs are shown in *E* (35). Below the doping level of ∼0.10, there is an opening of the nodal insulating gap. Above ∼0.10, the La-Bi2201 sample becomes superconducting with a d-wave superconducting gap. No gap is observed for the 0.105 sample because the superconducting gap size is zero along the nodal direction. (*F*) Fermi surface mapping near M2 point for the FeSe 0.076 sample. The dashed green circle schematically shows the underlying Fermi surface. (*G*) Symmetrized EDCs measured on the four Fermi momenta (marked by white solid circles in *F*) on the underlying Fermi surface in *F*. Red arrows indicate the position of the energy gap.

sharp peak at high carrier concentration like $x = 0.114$ (Fig. 2*B*). To check on possible gap opening, we divided out the Fermi distribution function from the photoemission intensity plots and highlight the near–Fermi-level energy region in Fig. 2*A*. The spectral weight is suppressed at low carrier concentration that indicates a gap opening. The spectral weight suppression gets weaker with increasing carrier concentration, and the gap appears to be closed for the $x = 0.089$ sample. However, further increase of the carrier concentration leads to a clear reopening of an energy gap with much reduced spectral weight at the Fermi level. To quantitatively keep track on the gap size change, the original EDCs (Fig. 2*B*) are symmetrized and shown in Fig. 2*D*. The symmetrization procedure can remove the effect of the Fermi distribution function and provides an intuitive way of discerning a gap opening (40). It is clear from Fig. 2*D* that, when the carrier concentration is low, there is a gap opening manifested by a spectral dip at the Fermi level. When the carrier concentration increases, the gap size, measured by the half-distance between the EDC peaks, gets smaller and closes at the carrier concentration of 0.089. Reopening of the energy gap is also evident as seen in the samples with carrier concentration of 0.098 and 0.114. For comparison, Fig. 2*C* shows EDCs of La-Bi2201 at various doping levels, and the corresponding symmetrized EDCs are shown in Fig. 2*E*. The S phase in the single-layer FeSe/$SrTiO_3$ film shows similar behaviors in its spectral line shape evolution with the carrier concentration compared with the La-Bi2201 system (35) as well as other cuprate systems (34).

The two gaps observed in the S phase of the single-layer FeSe/$SrTiO_3$ films, one that opens at carrier concentration lower than 0.089 and the other that opens at carrier concentration higher than 0.089, exhibit different temperature dependence (Fig. 3). The high carrier concentration energy gap shows a clear temperature dependence; it closes above a critical temperature (∼40 K in Fig. 3*I* for the 0.098 sample). Its gap size as a function of temperature follows a Bardeen–Cooper–Schrieffer (BCS)-like form (Fig. 3*J*). These observations, together with its strong coherence peak (Fig. 3*I*) and the particle-hole symmetry observed before (20–22), strongly indicate that this represents most likely a superconducting gap. On the other hand, the low carrier concentration energy gap behaves differently in a couple of aspects. First, the EDC peak is relatively broad at all temperatures; thermal broadening makes it even weaker at high temperature (Fig. 3*G*, 0.076 sample). Second, the gap size shows little temperature dependence until the highest temperature we have measured (75 K in Fig. 3*H* for the 0.076 sample). Fig. 3 *A*–*F* show the temperature evolution of the band structure measured along the momentum cut near M2 (as shown in Fig. 1*O*) for the 0.076 sample; the Fermi distribution function has been divided out to see part of the band above the Fermi level. Over the temperature range we measured, the spectral weight near the Fermi level is suppressed, signaling the opening of an energy gap. Third, the gap size can be rather large, up to ∼50 meV for the sample with a carrier concentration less than 0.073, which is much larger than the largest superconducting gap observed so far in the single-layer FeSe/$SrTiO_3$ film (∼20 meV) (19, 21, 22).

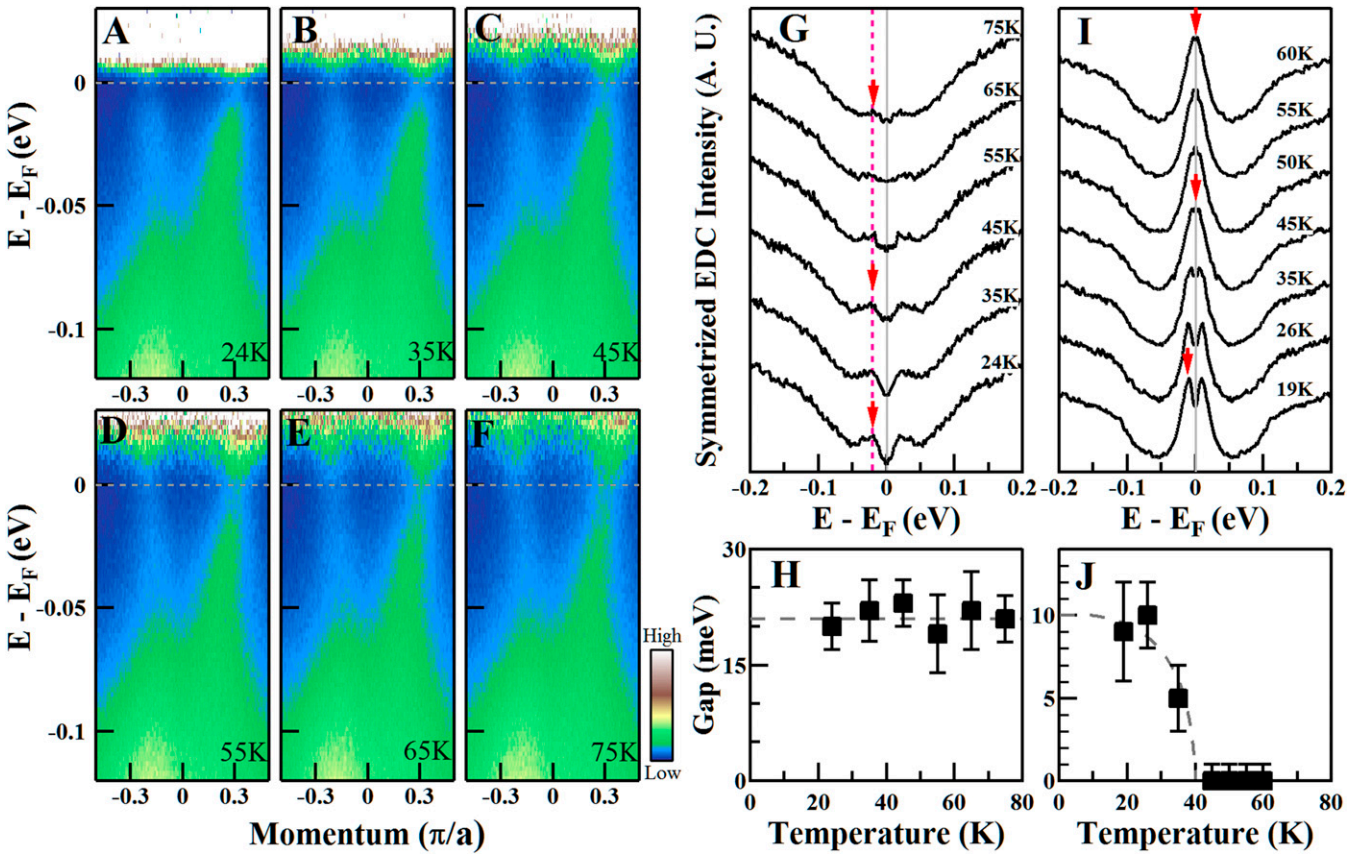

Fig. 3. Different temperature dependence of the two energy gaps for the S phase in the single-layer FeSe/$SrTiO_3$ film. (*A*–*F*) Photoemission intensity plots of the FeSe 0.076 sample measured along the momentum cut near M2 shown in Fig. 1*O* at 24, 35, 45, 55, 65, and 75 K, respectively. To observe part of the band above the Fermi level, the images are divided by the corresponding Fermi distribution function at different temperatures. A gap opening can be seen from the suppression of the spectral weight at the Fermi level, which persists from 24 to 75 K. (*G*) Symmetrized EDCs at the Fermi momentum k_F measured on the FeSe 0.076 sample at various temperatures. The red arrows indicate the position of the energy gap. The variation of the energy gap at different temperatures is shown in *H*. Over the temperature range we measured, the gap size shows little change with temperature. (*I*) Symmetrized EDCs at the Fermi momentum k_F measured on the FeSe 0.098 sample at various temperatures. The variation of the gap size at different temperatures is shown in *J*. It decreases with increasing temperature and closes above ~40 K. The gap variation with temperature follows a BCS-like form (dashed line).

These different behaviors indicate that the low carrier concentration energy gap is distinct from the superconducting gap. On the other hand, the broad EDC peaks, weak temperature dependence of the gap, and its relatively large size compared with the superconducting gap are similar to those observed in the insulating heavily-underdoped cuprates (34, 35). Therefore, we believe the low carrier concentration energy gap is more consistent with an insulating gap. We have also examined the momentum dependence of this insulating gap. As shown in Fig. 2*G*, within the experimental uncertainty, the gap size changes little along the "Fermi surface," 20~25 meV for the 0.076 sample at several Fermi momenta shown in Fig. 2*F*. This seems to be consistent with an isotropic insulating gap, although we caution that the determination of the insulating gap size involves relatively larger uncertainty because the EDC peaks are much weaker and broader than those in the superconducting samples.

The above electronic evidence clearly indicates that, at low carrier concentration, the S phase of the single-layer FeSe/$SrTiO_3$ film shows an insulating behavior. Its gap size decreases with increasing carrier concentration, and near the carrier concentration of 0.089, the insulating gap approaches zero. Right after this carrier concentration, superconductivity starts to emerge. Such an evolution is schematically summarized in Fig. 4*A*, together with the superconducting region at higher carrier concentration (21). This leads to a critical concentration near $x = 0.089$ at which an insulator–superconductor crossover occurs in the S phase. For comparison, we also include the phase diagram of the La-Bi2201 system where a clear insulator–superconductor transition has been recently identified near the doping level of 0.10 (Fig. 4*B*) (35). It is interesting to note that the band structure (Fig. 1), the EDCs and gap opening (Fig. 2), and the phase diagram (Fig. 4) show many similarities between the S phase of the single-layer FeSe/$SrTiO_3$ film and the La-Bi2201 system. On the other hand, there are some distinctions between single-layer FeSe/$SrTiO_3$ film and La-Bi2201. In the La-Bi2201 system, the parent compound is an antiferromagnetic insulator. With increasing doping, the nodal gap decreases to zero at ~0.10, together with the disappearance of the 3D antiferromagnetism. In the single-layer FeSe/$SrTiO_3$ film, it has been suggested that the N phase is possibly a magnetic phase (21), but it remains unclear whether the S phase at low carrier concentration (or zero carrier concentration) is magnetic or not. Another distinction is that La-Bi2201 is a quasi-2D system; it becomes 3D upon entering the superconducting state. On the other hand, the single-layer FeSe/$SrTiO_3$ is a genuine 2D system, remaining to be 2D even in the superconducting state.

Discussion

We notice the above gap evolution with carrier concentration is not simply from FeSe itself, because neither the insulating gap nor the ~20-meV superconducting gap was observed in bulk FeSe single crystal. Reduced dimensionality and interfacial

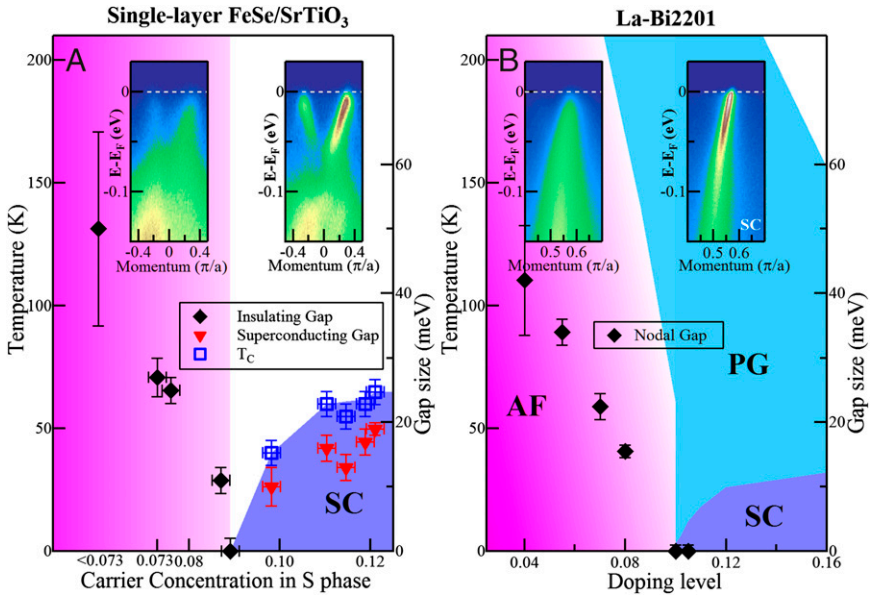

Fig. 4. Schematic phase diagrams of the S phase in the single-layer FeSe/$SrTiO_3$ film and La-Bi2201. (*A*) Phase diagram of the S phase in the single-layer FeSe/$SrTiO_3$ film that shows the decrease of the insulating energy gap (black solid diamond) with increasing carrier concentration at low doping side and the increase of the superconducting gap (red solid triangle) and the corresponding superconducting transition temperature T_c (blue empty square) with increasing carrier concentration at high doping side. There is an insulator–superconductor crossover near ~0.09 carrier concentration. (*B*) Phase diagram of La-Bi2201 showing a clear insulator–superconductor transition near 0.10 doping level. On the lower doping side, the nodal gap (black solid diamond) decreases with increasing doping and approaches zero at ~0.10 (35).

effect may play an important role. In fact, 2D systems with strong interfacial effect have attracted much attention by their exotic emergent phenomena. For example, in $LaAlO_3/SrTiO_3$ system, both a magnetic state (41) and a superconducting condensate (42) have been suggested as its ground states. Moreover, a pseudogap behavior and carrier density-induced insulator-to-superconductor transition have been observed, which are analogous to those in cuprates (43, 44). In our present case, the reduced dimensionality and strong interfacial effect have produced a new phenomenon in the iron-based superconductors: to our knowledge, the first observation of carrier density-induced insulator-to-superconductor crossover in the 2D FeSe/$SrTiO_3$ films, which is not seen in bulk iron-based superconductors so far.

In 2D systems, all electrons are believed to be localized even for the smallest levels of disorder (45). In principle, electrons can be spatially localized, either as a consequence of the random potential, which leads to Anderson localization (46), or of interactions, which results in a Mott insulator, or a combination of both (47). In the case of single-layer FeSe/$SrTiO_3$ films, during the annealing process, in addition to the electron concentration increase in the S phase (21), there are two other concomitant processes with the change of the relative amount of the N phase and S phase, and the change in the overall sample composition. During annealing, the initially dominant N phase gradually decreases with a concurrent increase of the S phase. It was also found that in the initial stage of annealing, some extra Se adatoms tend to appear on the surface of the FeSe film; it decreases with annealing, and in the final annealing stage, some Se vacancies can be formed (33). On the one hand, upon annealing, the amount of the N phase decreases, thus reducing the disorder effect to the transport properties of the S phase. On the other hand, during annealing, the disorder effect tends to first decrease with the removal of excess Se on the FeSe surface, and then increase from the formation of the Se vacancies within the FeSe layer. If the observed insulator–superconductor crossover is due to disorder-induced Anderson localization, the former case may be consistent with the picture, whereas the latter case with the enhanced disorder effect from the Se vacancy formation is inconsistent with the scenario.

An alternative scenario on the possible origin of the observed insulator–superconductor crossover in the S phase of the single-layer FeSe/$SrTiO_3$ film is that the electron correlation in this 2D system is strong so that the parent insulating phase may approach a Mott insulator. A number of our observations are in agreement with this possibility. (1). The single-layer FeSe/$SrTiO_3$ film may exhibit the strongest electron correlation among all of the iron-based compounds. It has been theoretically proposed that the iron-based superconductors may be on the verge of the doped Mott insulator (11, 15), and experimentally it has been shown that the iron pnictides, like $BaFe_2As_2$, exhibit moderately strong electron correlation (48). Further calculations indicate that the electron correlation in the iron-chalcogenides, like FeSe and FeTe, is stronger than that in the iron-pnictides (49). The electron correlation in the single-layer FeSe/$SrTiO_3$ film can be further enhanced by its two-dimensionality compared with its 3D bulk form. Moreover, the tensile stress exerted on the FeSe film from the $SrTiO_3$ substrate (19, 22) will also lead to the enhancement of the electron correlation (2). In a multiorbital system like the iron-based compounds, the carrier density-induced Mott transition may be realized in an orbital-selective fashion. In the iron-based compounds, depending on the electron repulsion and the relative bandwidth of each orbital, different orbitals may exhibit quite disparate behaviors, with some of them behaving like a Mott insulator while the other remains like a metal (50). Such an orbital-selective Mott transition has been examined in $A_xFe_{2-y}Se_2$ superconductor (51) where it is found that the d_{xy} orbital is responsible for such a Mott transition (51). This d_{xy} orbital forms an electron-like band near the M(π,π) point in the $A_xFe_{2-y}Se_2$ superconductor (51). In the S phase of the single-layer FeSe/$SrTiO_3$ film (Fig. 1 *A*–*G*), it is the same d_{xy} orbital that forms the electron-like band near M point. (3). In the copper-oxide superconductors, it is usually agreed that superconductivity arises from doping the Mott insulator (5). The similar behaviors of the insulator–superconductor crossover

observed in the S phase of the single-layer FeSe/$SrTiO_3$ film and in heavily underdoped La-Bi2201 (35) are consistent with the doping Mott insulator picture.

In summary, by systematic study on the carrier evolution of the S phase in the single-layer FeSe/$SrTiO_3$ films, we have observed the first example (to our knowledge) of a carrier density-induced insulator–superconductor crossover in the iron-based superconductors. The evolution shows strong similarity to the insulator–superconductor transition observed in the high temperature cuprate superconductors. Although further work needs to be done to pin down on the origin of the insulator–superconductor crossover, such as the Anderson localization or orbital selective Mott transition, our results point to the importance of two-dimensionality in giving rise to such a new phenomenon, which is not seen in its bulk counterpart. The reduced dimensionality, combined with the enhanced interfacial effect, may provide a new platform to explore for novel phenomena and high-temperature superconductivity.

Materials and Methods

The as-grown single-layer FeSe/$SrTiO_3$ films were prepared by the molecular beam epitaxy method and characterized by scanning tunneling microscope. The details of the sample preparation process and conditions can be found in ref. 19. The as-grown samples were consecutively annealed in ultrahigh vacuum at different temperatures and for different times as described before (21). After each annealing, ARPES measurements were carried out to keep track on the evolution of band structure, Fermi surface, and energy gap.

ARPES measurements were performed on our laboratory system equipped with a Scienta R4000 analyzer and a helium lamp with a photon energy of 21.218 eV as the light source (52). The energy resolution was set at 10~20 meV for the band structure measurements and Fermi surface mapping and at 4~10 meV for the gap measurements. The angular resolution for the measurements is ~0.3°. The Fermi level is determined by measuring on a clean polycrystalline gold, which is electrically connected to the sample. The measurements were carried out in ultrahigh vacuum with a base pressure better than 5×10^{-11} torr.

ACKNOWLEDGMENTS. X.J.Z. is thankful for financial support from the National Natural Science Foundation of China (11190022, 11334010, and 11374335), the Ministry of Science and Technology (MOST) of China (973 Programs 2011CB921703 and 2011CBA00110), and the Strategic Priority Research Program (B) of the Chinese Academy of Sciences via Grant XDB07020300. Q.K.X. and X.C.M. are thankful for support from the MOST of China (Programs 2009CB929400 and 2012CB921702).

1. Johnston DC (2010) The puzzle of high temperature superconductivity in layered iron pnictides and chalcogenides. *Adv Phys* 59(6):803–1061.
2. Paglione J, Greene RL (2010) High-temperature superconductivity in iron-based materials. *Nat Phys* 6(9):645–658.
3. Stewart GR (2011) Superconductivity in iron compounds. *Rev Mod Phys* 83(4): 1589–1652.
4. Wang F, Lee DH (2011) The electron-pairing mechanism of iron-based superconductors. *Science* 332(6026):200–204.
5. Lee PA, Nagaosa N, Wen XG (2006) Doping a Mott insultaor: Physics of high temperature superconductivity. *Rev Mod Phys* 78(1):17–85.
6. Singh DJ, Du M-H (2008) Density functional study of $LaFeAsO_{(1-x)}F_{(x)}$: A low carrier density superconductor near itinerant magnetism. *Phys Rev Lett* 100(23):237003.
7. Mazin II, Singh DJ, Johannes MD, Du MH (2008) Unconventional superconductivity with a sign reversal in the order parameter of $LaFeAsO_{1-x}F_x$. *Phys Rev Lett* 101(5): 057003.
8. Kuroki K, et al. (2008) Unconventional pairing originating from the disconnected Fermi surfaces of superconducting $LaFeAsO_{1-x}F_x$. *Phys Rev Lett* 101(8):087004.
9. Graser S, et al. (2009) Near-degeneracy of several pairing channels in multiorbital models for the Fe pnictides. *New J Phys* 11:025016.
10. Wang F, Zhai H, Ran Y, Vishwanath A, Lee DH (2009) Functional renormalization-group study of the pairing symmetry and pairing mechanism of the FeAs-based high-temperature superconductor. *Phys Rev Lett* 102(4):047005.
11. Si Q, Abrahams E (2008) Strong correlations and magnetic frustration in the high T_c iron pnictides. *Phys Rev Lett* 101(7):076401.
12. Seo K, Bernevig BA, Hu J (2008) Pairing symmetry in a two-orbital exchange coupling model of oxypnictides. *Phys Rev Lett* 101(20):206404.
13. Chen W-Q, Yang KY, Zhou Y, Zhang FC (2009) Strong coupling theory for superconducting iron pnictides. *Phys Rev Lett* 102(4):047006.
14. Kou SP, et al. (2009) Coexistence of itinerant electrons and local moments in iron-based superconductors. *Europhys Lett* 88(1):17010.
15. Dai J, Si Q, Zhu JX, Abrahams E (2009) Iron pnictides as a new setting for quantum criticality. *Proc Natl Acad Sci USA* 106(11):4118–4121.
16. Yu R, Si QM (2011) Mott transition in multiorbital models for iron pnictides. *Phys Rev B* 84(23):235115.
17. Zhou Y, et al. (2011) Theory for superconductivity in $(Tl,K)Fe_xSe_2$ as a doped Mott insulator. *Europhys Lett* 95(1):17003.
18. Hu JP, et al. (2012) S-4 symmetric microscopic model for iron-based superconductors. *Phys Rev X* 2(2):021009.
19. Wang QY, et al. (2012) Interface-induced high-temperature superconductivity in single unit-cell FeSe films on $SrTiO_3$. *Chin Phys Lett* 29(3):037402.
20. Liu D, et al. (2012) Electronic origin of high-temperature superconductivity in single-layer FeSe superconductor. *Nat Commun* 3:931.
21. He S, et al. (2013) Phase diagram and electronic indication of high-temperature superconductivity at 65 K in single-layer FeSe films. *Nat Mater* 12(7):605–610.
22. Tan S, et al. (2013) Interface-induced superconductivity and strain-dependent spin density waves in FeSe/$SrTiO_3$ thin films. *Nat Mater* 12(7):634–640.
23. Zhang WH, et al. (2014) Direct observation of high temperature superconductivity in one-unit-cell FeSe films. *Chin Phys Lett* 31(1):017401.
24. Deng LZ, et al. (2013) The Meissner and mesoscopic superconducting states in 1-4 unit-cell FeSe-films up to 80 K. arXiv:1311.6459.
25. Lee JJ, et al. (2013) Evidence for pairing enhancement in single unit cell FeSe on $SrTiO_3$ due to cross-interfacial electron-phonon coupling. arXiv:1312.2633.
26. Peng R, et al. (2014) Measurement of an enhanced superconducting phase and a pronounced anisotropy of the energy gap of a strained FeSe single layer in FeSe/Nb: $SrTiO_3/KTaO_3$ heterostructures using photoemission spectroscopy. *Phys Rev Lett* 112(10):107001.
27. Ge JF, et al. (2014) Superconductivity in single-layer films of FeSe with a transition temperature above 100 K. *Nat Mater*, 10.1038/nmat4153.
28. Liu K, et al. (2012) Atomic and electronic structures of FeSe monolayer and bilayer thin films on $SrTiO_3$(001): First-principles study. *Phys Rev B* 85(23):235123.
29. Xiang YY, et al. (2012) High-temperature superconductivity at the FeSe/$SrTiO_3$ interface. *Phys Rev B* 86(13):134508.
30. Bazhirov T, Cohen ML (2013) Effects of charge doping and constrained magnetization on the electronic structure of an FeSe monolayer. *J Phys Condens Matter* 25(10): 105506.
31. Zheng FW, et al. (2013) Antifferomagnetic FeSe monolayer on $SrTiO_3$: The charge doping and electric field effects. arXiv:1302.2996.
32. Cao HY, et al. (2014) Interfacial effects on the spin density wave in FeSe/$SrTiO_3$ thin films. *Phys Rev B* 89(1):014501.
33. Zhang WH, et al. (2014) Interface charge doping effects on superconductivity of single-unit-cell FeSe films on $SrTiO_3$ substrates. *Phys Rev B* 89(6):060506.
34. Yoshida T, et al. (2003) Metallic behavior of lightly doped $La_{2-x}Sr_xCuO_4$ with a Fermi surface forming an arc. *Phys Rev Lett* 91(2):027001.
35. Peng Y, et al. (2013) Disappearance of nodal gap across the insulator-superconductor transition in a copper-oxide superconductor. *Nat Commun* 4:2459.
36. Vishik IM, et al. (2012) Phase competition in trisected superconducting dome. *Proc Natl Acad Sci USA* 109(45):18332–18337.
37. Razzoli E, et al. (2013) Evolution from a nodeless gap to d(x(2)-y(2))-wave in underdoped La(2-x)Sr(x)CuO_4. *Phys Rev Lett* 110(4):047004.
38. Lupi S, et al. (2009) Far-infrared absorption and the metal-to-insulator transition in hole-doped cuprates. *Phys Rev Lett* 102(20):206409.
39. Liu GD, et al. (2009) Band structure reorganization across the magnetic transition in $BaFe_2As_2$ seen via high-resolution angle-resolved photoemission. *Phys Rev B* 80(13): 134519.
40. Norman MR, et al. (1998) Phenomenology of the low-energy spectral function in high-T_c superconductors. *Phys Rev B* 57(18):R11093–R11096.
41. Brinkman A, et al. (2007) Magnetic effects at the interface between non-magnetic oxides. *Nat Mater* 6(7):493–496.
42. Reyren N, et al. (2007) Superconducting interfaces between insulating oxides. *Science* 317(5842):1196–1199.
43. Richter C, et al. (2013) Interface superconductor with gap behaviour like a high-temperature superconductor. *Nature* 502(7472):528–531.
44. Caviglia AD, et al. (2008) Electric field control of the $LaAlO_3/SrTiO_3$ interface ground state. *Nature* 456(7222):624–627.
45. Abrahams E, et al. (1979) Scaling theory of localization: Absence of quantum diffusion in two dimensions. *Phys Rev Lett* 42(10):673–676.
46. Anderson PW (1958) Absence of diffusion in certain random lattices. *Phys Rev* 109(5): 1492–1505.
47. Liu Y, Haviland DB, Nease B, Goldman AM (1993) Insulator-to-superconductor transition in ultrathin films. *Phys Rev B* 47(10):5931–5946.
48. Qazibash MM, et al. (2009) Electronic correlations in the iron pnictides. *Nat Phys* 5(9): 647–650.
49. Yin ZP, Haule K, Kotliar G (2011) Kinetic frustration and the nature of the magnetic and paramagnetic states in iron pnictides and iron chalcogenides. *Nat Mater* 10(12): 932–935.
50. Yu R, Si Q (2013) Orbital-selective Mott phase in multiorbital models for alkaline iron selenides K1-xFe2-ySe2. *Phys Rev Lett* 110(14):146402.
51. Yi M, et al. (2013) Observation of temperature-induced crossover to an orbital-selective Mott phase in $A_{(x)}Fe_{(2-y)}Se_2$ (A=K, Rb) superconductors. *Phys Rev Lett* 110(6): 067003.
52. Liu G, et al. (2008) Development of a vacuum ultraviolet laser-based angle-resolved photoemission system with a superhigh energy resolution better than 1 meV. *Rev Sci Instrum* 79:023105.

Supplementary Information for

Electronic Evidence of an Insulator-Superconductor Crossover in Single-Layer FeSe/$SrTiO_3$ Films

Junfeng He[a,1], Xu Liu[a,1], Wenhao Zhang[b,c,1], Lin Zhao[a,1], Defa Liu[a], Shaolong He[a], Daixiang Mou[a], Fangsen Li[c], Chenjia Tang[b,c], Zhi Li[c], Lili Wang[c], Yingying Peng[a], Yan Liu[a], Chaoyu Chen[a], Li Yu[a], Guodong Liu[a], Xiaoli Dong[a], Jun Zhang[a], Chuangtian Chen[d], Zuyan Xu[d], Xi Chen[b], Xucun Ma[c,2], Qikun Xue[b,2], and X. J. Zhou[a,e,2]

[a] *National Lab for Superconductivity, Beijing National Laboratory for Condensed Matter Physics, Institute of Physics, Chinese Academy of Sciences, Beijing 100190, China*

[b] *State Key Lab of Low-Dimensional Quantum Physics, Department of Physics, Tsinghua University, Beijing 100084, China*

[c] *Beijing National Laboratory for Condensed Matter Physics, Institute of Physics, Chinese Academy of Sciences, Beijing 100190, China*

[d] *Technical Institute of Physics and Chemistry, Chinese Academy of Sciences, Beijing 100190, China*

[e] *Collaborative Innovation Center of Quantum Matter, Beijing 100871, China*

(Dated: August 17, 2014)

1. Determination of the carrier concentration of the S phase by measuring the area of electron Fermi pocket.

The electronic structure of the S phase in the single-layer FeSe/$SrTiO_3$ is characterized by electron pockets near the M(π,π) zone corners without any Fermi crossing near the zone center. Thus the area of the electron pocket can be used to estimate the electron carrier concentration of the S phase. With annealing, the size of the pocket gets larger which indicates an increase of the carrier concentration. Typical electron Fermi pocket near M2 is shown in an expanded scale for x=0.089 (Fig. S1a) and x=0.114 (Fig. S1b). As a guide to the eye, the gray circle which fits the electron pocket in sample x=0.114 (b) is also duplicated in (a) as dashed gray circles. The carrier concentration x is estimated by the area of the circles which fit the electron Fermi pockets (assuming two electron pockets at a given M point) with an error bar of $\pm$0.003 arising from the uncertainty in determining the area of the pocket. The correspondence of the carrier concentration and the annealing sequence is similar to that reported before (Fig. 2h in [1]).

2. Picking up dominant signal for the S phase by taking advantage of the photoemission matrix element effect.

As shown in Fig. S2, for the measurement geometry we used, we can selectively pick up dominant signals for the S phase when it coexists with the N phase in the intermediate annealing process. For the cut near M2 (Fig. S2e), the signal is dominated by the S phase which shows a representative electron-like band (original in Fig. S2a and second derivative image in Fig. S2c). On the other hand, for the cut near M3 (Fig. S2f), the signal is dominated by the N phase which is characterized by a hole-like band, in addition to the electron-like band from the S phase. Therefore, the signal of the momentum cut near M2 is dominated by the S phase with little signal from the N phase. It is ideal for probing the evolution of the electronic structure with doping for the S phase when it coexists with the N phase.

3. Raw images and symmetrized photoemission spectra (EDCs) for the single-layer FeSe/$SrTiO_3$ films at different annealing sequences.

Fig. S3 shows original data [Fig. S3(a-g)] and the corresponding symmetrized EDCs [Fig. S3(h-n)] of the single-layer FeSe/$SrTiO_3$ film at different annealing sequences. The

carrier concentrations of the S phase in the samples are the same as those in Fig. 1(A-G). From the symmetrized EDCs, one can identify the energy gap. The red curves are the EDCs at the Fermi momentum k_F, the same as those shown in Fig. 2.

---

[1] He S, et al. (2013) Phase diagram and electronic indication of high-temperature superconductivity at 65 K in single-layer FeSe films. *Nat Mater* 12(7):605-610.

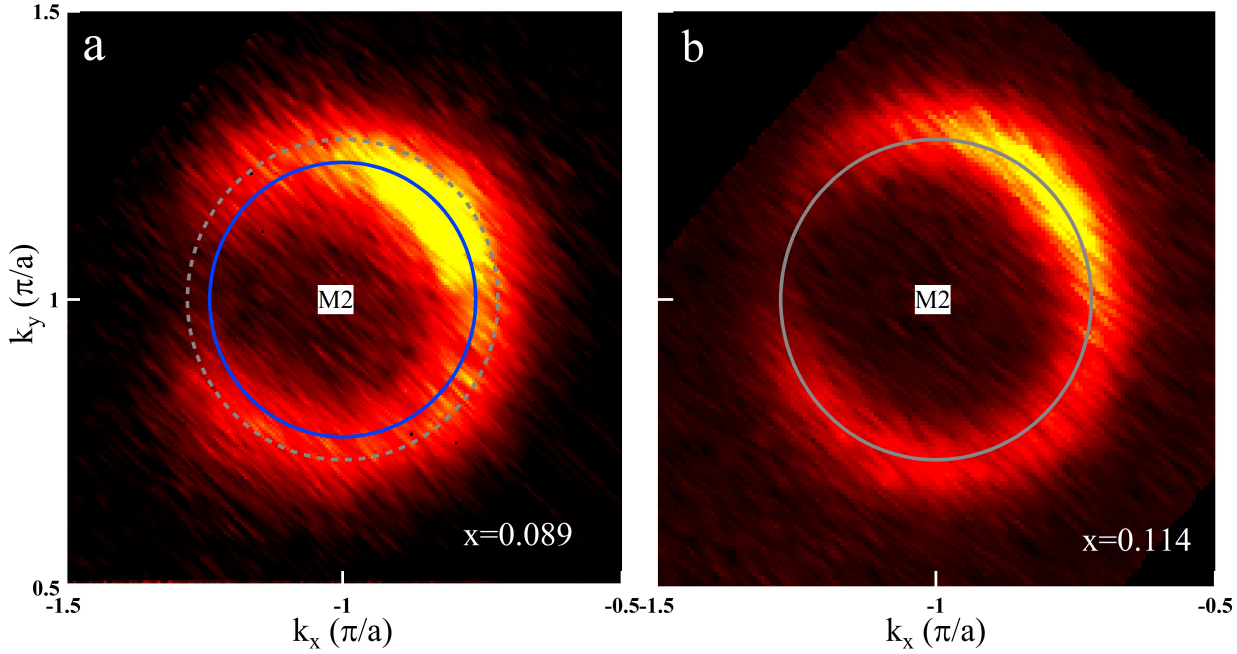

Fig. S 1: **Electron Fermi pocket near M2 for the single-layer FeSe/$SrTiO_3$ at two different annealing sequences.** The electron carrier concentration can be estimated from the area of the Fermi pocket. (a), x=0.089 and (b), x=0.114. Blue and gray circles indicate the area of each Fermi pocket.

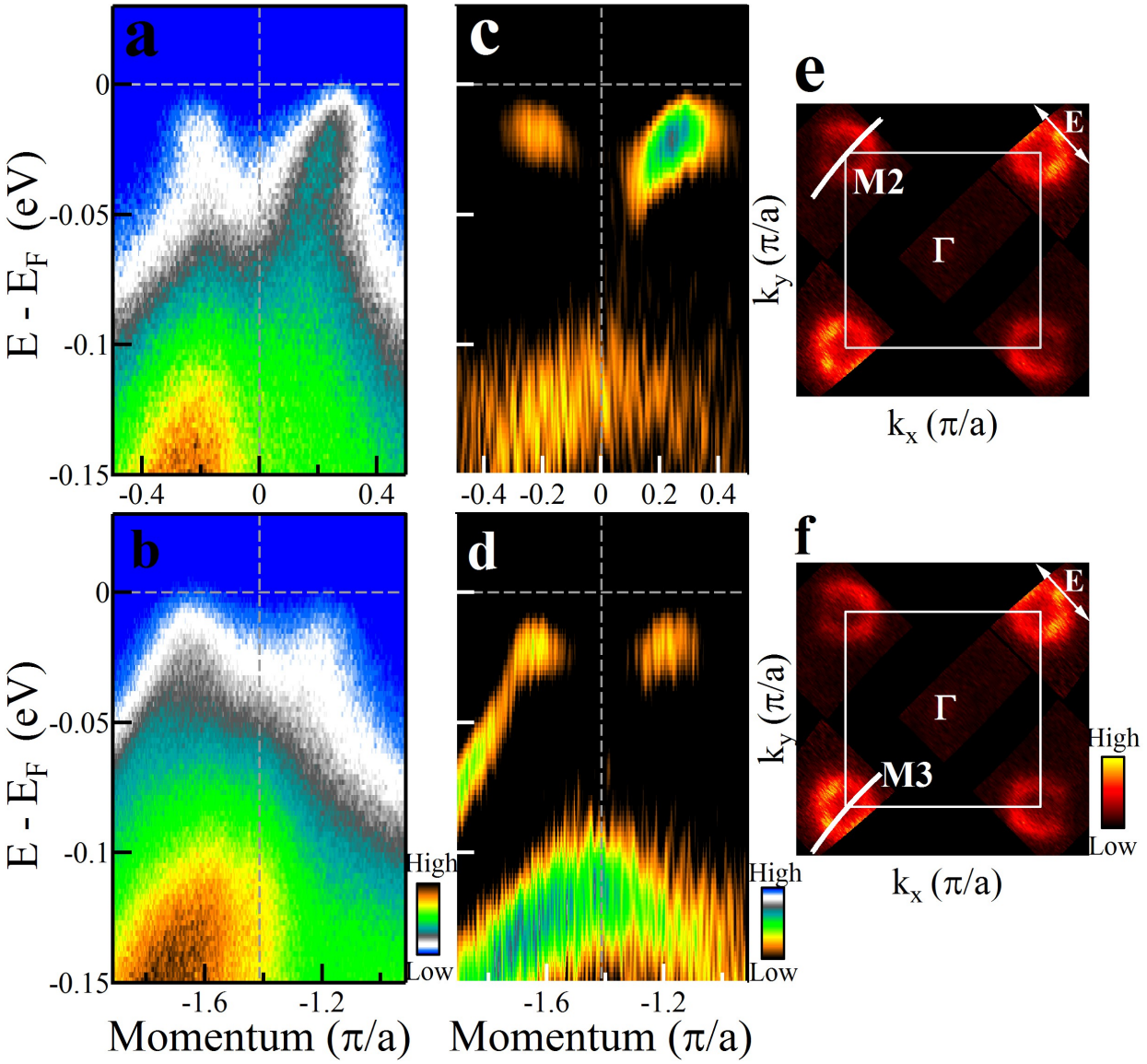

Fig. S 2: **Matrix element effect on the signal obtained from the S phase and the N phase.** Photoemission images measured on a FeSe 0.076 sample near M2(a) and M3(b) and their corresponding EDC second derivative images [(c) and (d)]. (e) and (f) show the location of the momentum cuts on the Fermi surface. The signal of the cut near M2 is dominated by the S phase because the hole-like band which represents N phase can only be seen in (b) and (d), but not in (a) and (c). The double-head arrow in the upper-right corner of (e) and (f) shows the electric field vector of the incident light.

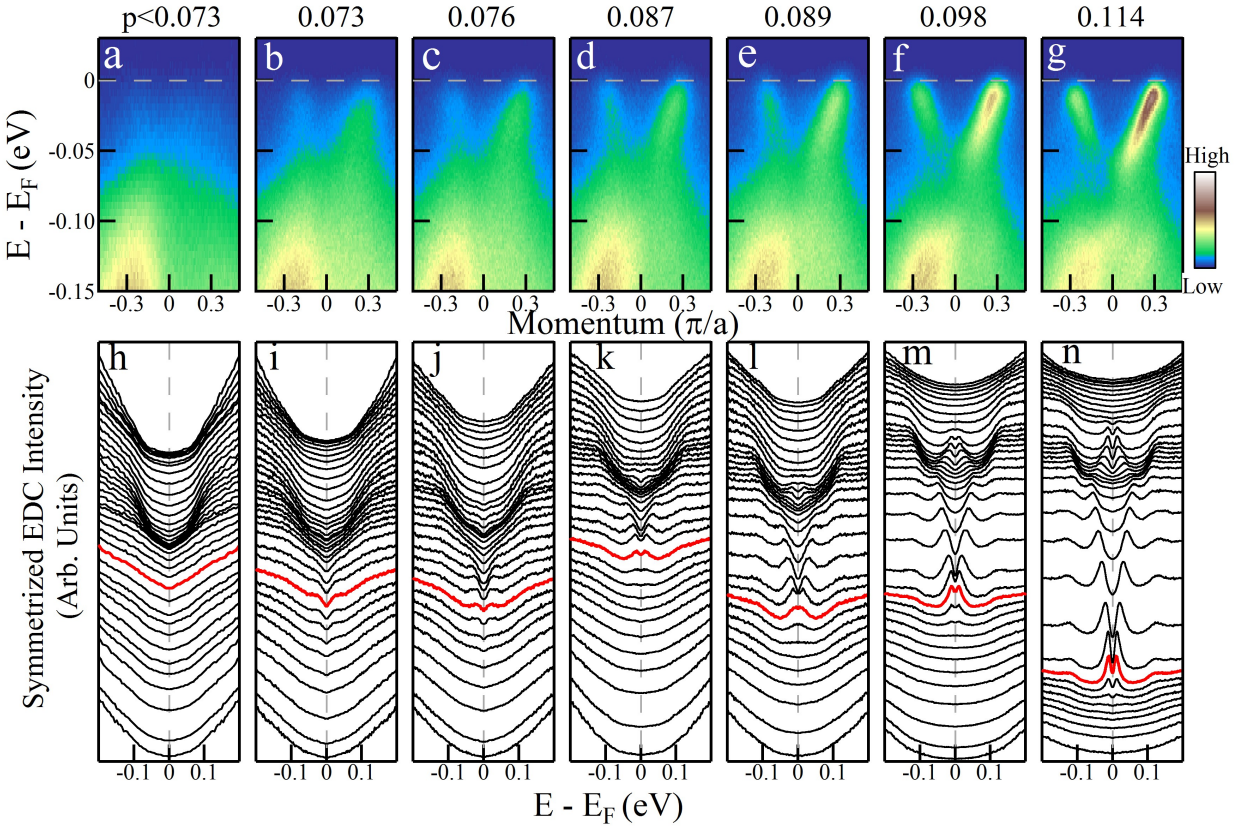

Fig. S 3: **Original images and symmetrized energy distribution curves(EDCs) for single-layer FeSe/$SrTiO_3$ films at different annealing sequences.** (a-g). Photoemission intensity plots of the single-layer FeSe samples with the carrier concentration of the S phase as <0.073, 0.073, 0.076, 0.087, 0.089, 0.098, 0.114, respectively. (h-n). The corresponding symmetrized EDCs in each measurement. The red curves represent the EDCs at the Fermi momentum k_F.